Highly-efficient 2.3 µm Thulium lasers based on a high-phonon-energy crystal: Evidence of vibronic-assisted emissions

Pavel Loiko,[1] Esrom Kifle,[1] Lauren Guillemot,[1] Jean-Louis Doualan,[1] Florent Starecki,[1] Alain Braud,[1] Magdalena Aguilo,[2] Francesc Diaz,[2] Valentin Petrov[3], Xavier Mateos[2], and Patrice Camy[1,*]

[1]Centre de Recherche sur les Ions, les Matériaux et la Photonique (CIMAP), UMR 6252 CEA-CNRS-ENSICAEN, Université de Caen Normandie, 6 Boulevard du Maréchal Juin, 14050 Caen Cedex 4, France

[2]Universitat Rovira i Virgili (URV), Física i Cristal·lografia de Materials i Nanomaterials (FiCMA-FiCNA)-EMaS, Marcel.li Domingo 1, 43007 Tarragona, Spain

[3]Max Born Institute for Nonlinear Optics and Short-Pulse Spectroscopy, 2A Max-Born-Str., 12489 Berlin, Germany

**Corresponding author: patrice.camy@ensicaen.fr*

Received XX Month XXXX; revised XX Month, XXXX; accepted XX Month XXXX; posted XX Month XXXX (Doc. ID XXXXX); published XX Month XXXX

We report on highly-efficient and power-scalable laser operation in a thulium-doped high-phonon energy crystal (monoclinic double tungstate, $KLu(WO_4)_2$) on the $^3H_4 \rightarrow {}^3H_5$ Tm^{3+} transition giving rise to the short-wave infrared emission at ~2.3 µm. A 3 at.% Tm doped crystal generated a maximum continuous-wave output power of 1.12 W at ~2.22 and 2.29 µm with a record-high slope efficiency of 69.2% (*vs.* the absorbed pump power), a slightly multimode beam ($M^2_{x,y}$ = 2.2 and 2.6) and a linear laser polarization. The ~2.3 µm laser outperformed the one operating on the conventional $^3F_4 \rightarrow {}^3H_6$ transition (at ~1.95 µm). The effect of the Tm concentration on the ~2.3 µm laser performance indicates a gradually increasing pump quantum efficiency for the $^3H_4$ upper laser level with the Tm doping. For the 3 at.% Tm doped crystal, it reached 1.8±0.1 (almost two-for-one pump process) which is attributed to efficient energy-transfer upconversion. We discuss the physical nature of the laser emissions occurring at intermediate wavelengths between the electronic $^3H_4 \rightarrow {}^3H_5$ and $^3F_4 \rightarrow {}^3H_6$ transitions and highlight the role of electron-phonon coupling (vibronic processes) in the appearance of such laser lines. This allowed us to better understand the near- and mid-infrared emission from thulium ions which can be used in broadly tunable and fs mode-locked 2-2.3 µm lasers. © 2020 Optical Society of America

1. INTRODUCTION

In recent years, coherent light sources emitting near 2.3 µm in the short-wavelength infrared (SWIR) spectral range are attracting increasing attention. Such emission falls into the atmosphere transparency window with weak water vapor absorption containing at the same time absorption lines of atmospheric pollutants, i.e., hydrogen fluoride (HF), carbon monoxide (CO), methane (CH_4) or formaldehyde (H_2CO). Consequently, ~2.3 µm lasers find applications in gas sensing in the atmosphere [1,2] and optical metrology of combustion processes [3]. They are also promising for non-invasive glucose ($C_6H_{12}O_6$) blood measurements [4]. Potentially, ultrafast ~2.3 µm lasers can be used for further frequency conversion into the mid-IR [5].

There exist several possibilities to obtain emission near 2.3 µm from solid-state lasers. Cr^{2+}-doped II-IV group materials - zinc chalcogenides (ZnS, ZnSe) - give rise to a broadly tunable laser emission covering the desired wavelength [6]. Sorokina *et al.* reported on a continuous-wave (CW) Cr^{2+}:ZnS laser delivering 100 mW at ~2.35 µm with a slope efficiency of 16%, tunable between 2.19 - 2.47 µm [7]. Further power scaling reaching multi-watt regime at improved slope efficiency were demonstrated later on [6,8]. Mode-locked (ML) Cr^{2+}:ZnS and Cr^{2+}:ZnSe lasers generating femtosecond (fs) pulses are also known [9, 10]. However, the fabrication of high-optical quality zinc chalcogenide crystals and ceramics is complex. Moreover, such lasers require special pump sources, such as Co^{2+} lasers at ~1.67 µm or Tm^{3+} fiber or bulk lasers at ~1.9 µm.

Another possibility is the use of semiconductor structures (GaInAs on InP or GaInAsSb on GaSb), e.g., in diode lasers [11] or Vertical-Cavity Surface-Emitting Lasers (VECSELs) [12]. Besides the relatively complex design and fabrication methods, the power scaling capabilities of such lasers (single-emitters) are limited. Geerlings *et al.* presented a GaSb-based diode laser generating 16.5 mW at ~2.23 µm with a wavelength tunability between 2.21 – 2.39 µm [11]. The output power can be scaled reaching watt-level in array configuration however with a trade-off on spatial quality [13]. In addition, the ultrafast operation of such lasers has been poorly studied.

Finally, ~2.3 μm emission can be obtained using thulium (Tm^{3+}) doped materials based on the $^3H_4 \rightarrow {}^3H_5$ quasi-four-level transition, Fig. 1(a). This laser scheme has been long known both for bulk [14] and fiber [15] lasers. However, it was considered to be inefficient and the $^3F_4 \rightarrow {}^3H_6$ transition at ~2 μm received much more attention [16]. At a glance, there are several difficulties in realizing ~2.3 μm Tm lasers, i.e., (i) relatively short radiative lifetime of the upper laser level ($^3H_4$) and low luminescence branching ratio for the $^3H_4 \rightarrow {}^3H_5$ transition [14], (ii) multi-phonon non-radiative (NR) relaxation from this state in high-phonon energy (oxide) host materials, (iii) strong self-quenching of the luminescence lifetime with Tm doping due to an efficient cross-relaxation process, $^3H_4(Tm_1) + {}^3H_6(Tm_2) \rightarrow {}^3F_4(Tm_1) + {}^3F_4(Tm_2)$, for neighboring Tm^{3+} ions [17], (iv) energy-migration to impurities from the $^3H_4$ state at high Tm^{3+} doping levels [18], and (v) highly probable colasing on the high-gain $^3F_4 \rightarrow {}^3H_6$ transition. The advantage of ~2.3 μm lasers based on Tm^{3+} ions (as compared to other sources emitting in this spectral range) is the availability of pump sources (e.g., AlGaAs laser diodes [19] whose emission at ~0.8 μm well overlaps with an intense and broad $^3H_6 \rightarrow {}^3H_4$ Tm^{3+} absorption band) and laser gain media (e.g., $Tm:LiYF_4$ single-crystals [20] or Tm:ZBLAN glass fibers [21]).

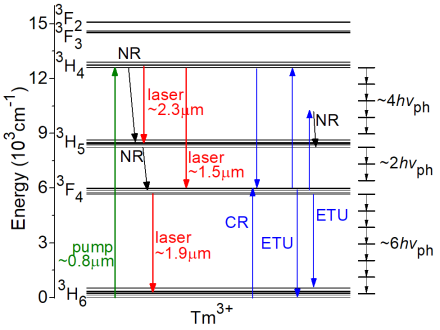

Fig. 1. Energy level scheme of the Tm^{3+} ion in the high-phonon-energy monoclinic double tungstate crystal $KLu(WO_4)_2$ (after [22]), showing the pump transition (*green arrow*), laser transitions (*red arrows*), cross-relaxation (CR) and energy-transfer upconversion (ETU). NR is the non-radiative decay. The equally separated *horizontal dashes* show the average number of high-energy phonons ($h\nu_{ph}$) needed to bridge the energy gaps between the multiplets involved in laser emission.

The above considerations however greatly limited the selection of active gain media for bulk ~2.3 μm Tm lasers from the point of view of the host matrix (only low-phonon energy crystals, e.g., fluorides) and the Tm doping level (preferably low, to prevent self-quenching of the $^3H_4$ lifetime). Thus, in most of the previous studies, mainly $Tm:LiYF_4$ crystals with relatively low doping levels were studied, see, e.g., [19,20].

Pinto *et al.* reported on a CW $Tm:LiYF_4$ laser delivering 0.22 W at 2.30 μm with a slope efficiency of 15 % and achieved a wavelength tuning between 2.20 - 2.46 μm [20]. ML $Tm:LiYF_4$ lasers operating on the $^3H_4 \rightarrow {}^3H_5$ transition were reported in [23,24]. The shortest pulses were achieved by Canbaz *et al.* (514 fs at 2.30 μm) from a Kerr-lens ML laser operating at a repetition rate of 41.5 MHz [24]. The slope efficiency in such lasers has been rather low, well below the Stokes limit of $\eta_{StL} \approx$ 34% for $Tm:LiYF_4$. Only recently, we showed theoretically [25] and reported experimentally using fluoride crystals [25,26] that the slope efficiency of Tm lasers operating on the $^3H_4 \rightarrow {}^3H_5$ transition can overcome the Stokes limit and potentially approach $2\eta_{StL}$ owing to energy-transfer upconversion (ETU), $^3F_4(Tm_1) + {}^3F_4(Tm_2) \rightarrow {}^3H_6(Tm_1) + {}^3H_4(Tm_2)$, which becomes efficient at moderate Tm doping levels and acts against the CR by refilling the upper laser level. We also suggested that this mechanism may act in other Tm^{3+}-doped crystals.

Note that other pumping schemes for ~2.3 μm Tm lasers relying on the photon avalanche mechanism were also proposed, still leading to a relatively low laser efficiency [27,28].

Recently, we revisited well-known Tm^{3+}-doped oxide crystals ($Tm:Y_3Al_5O_{12}$, $Tm:YAlO_3$) regarding their potential for efficient 2.3 μm lasers [29,30]. We demonstrated a watt-level output from a $Tm:Y_3Al_5O_{12}$ laser operating on the $^3H_4 \rightarrow {}^3H_5$ transition: 1.07 W at ~2.19 and 2.32 μm with a slope efficiency of 46.3% [29]. However, both crystals are known for their relatively long radiative lifetimes of the $^3H_4$ state and moderate multi-phonon NR relaxation from this level. Interestingly, the use of $Tm:Y_3Al_5O_{12}$ (highest phonon energy of 857 cm^{-1}) raised the question of the role of vibronic emission for wavelengths between 2 and 2.3 μm.

In the present work, we demonstrate power-scalable and highly-efficient operation on the $^3H_4 \rightarrow {}^3H_5$ transition of a Tm laser based on another high-phonon energy oxide host, monoclinic double tungstate, and reveal the effect of the Tm doping concentration on the laser performance. As a material under study, we selected Tm^{3+}-doped $KLu(WO_4)_2$ [31]. So far, this crystal has been extensively studied for CW [32], Q-switched [33] and fs ML [34] lasers emitting at ~2 μm. Its spectroscopic features are high absorption and stimulated-emission cross-sections for polarized light, broad and intense emission bands, high quantum yield and weak concentration-quenching of the luminescence from the $^3F_4$ state, and efficient CR [22]. The host matrix also provides nearly athermal behavior for certain crystal cuts thus allowing for power scaling [32]. $KLu(WO_4)_2$ is known as a Raman-active material [35] with yet higher maximum phonon energy $h\nu_{ph}$ of ~907 cm^{-1}. Thus, the energy-gap law for the multi-phonon NR relaxation postulating that the rate of NR relaxation is weak if $\Delta E > 4h\nu_{ph}$ (ΔE is the energy-gap to the lower-lying multiplet) [36] is valid for both the $^3H_4$ and $^3F_4$ states, Fig. 1(a). So far, ~2.3 μm lasing from $Tm:KLu(WO_4)_2$ or its Tm^{3+}-doped isomorphs $KGd(WO_4)_2$ and $KY(WO_4)_2$ has never been demonstrated.

2. CRYSTAL GROWTH

The growth of $Tm:KLu(WO_4)_2$ crystals was addressed before [31]. Here, we briefly mention the key details. The crystals were grown by the Top Seeded Solution Growth Slow-Cooling (TSSG SC) method from the flux using potassium ditungstate ($K_2W_2O_7$) as a solvent [31]. An undoped seed oriented along the [010] direction was used to start the growth. The growth was performed in Pt crucibles using K_2CO_3, WO_3, Lu_2O_3 and Tm_2O_3 reagents. The concentration of Tm^{3+} ions was 0.5, 1.5 or 3.0 at.%. The temperature gradient in the solution was ~1 K/cm, the rotation speed of the seed was 40 rpm and the cooling rate was 0.1-0.3 K/h. The crystals had a slight pale-yellow coloration due to the Tm^{3+} doping. The actual Tm^{3+} doping concentration N_{Tm} in the crystals was determined by Electron Probe MicroAnalysis (EPMA), see Table 1.

Table 1. Parameters of the Thulium-doped Laser Elements

Doping, at.%	N_{Tm}, 10^{20} cm^{-3}	t, mm	Aperture, mm^2
0.5	0.35	9.30(N_g)	2.56(N_m)×3.12(N_p)
1.5	1.14	5.97(N_g)	3.72(N_m)×4.10(N_p)
3.0	2.41	4.91(N_g)	3.73(N_m)×4.09(N_p)

$Tm:KLu(WO_4)_2$ belongs to the monoclinic crystal class (sp. gr. C^6_{2h} – $C2/c$, No. 15). The lattice constants for 3 at.% Tm doping are a = 10.576 Å, b = 10.215 Å, c = 7.487 Å and the monoclinic angle β = 130.68° [22]. This crystal is optically biaxial. Its optical indicatrix was deeply characterized before [31,37]. Briefly, the three optical indicatrix axes (N_p, N_m and N_g) are selected according to the convention $n_p < n_m < n_g$ for the principal refractive indices, and are oriented as follows: the N_p axis is parallel to the ***b***-axis (the C_2 symmetry axis) and the N_m and N_g

ones are lying in the ***a*-*c*** plane ($\perp C_2$, the mirror plane). The angle N_g^***c*** = 18.5°, measured outside the monoclinic angle β [31]. At the wavelength of ~2.3 μm, the principal refractive indices calculated using the Sellmeier equations [37] are n_p = 1.984, n_m = 2.014 and n_g = 2.061.

The rectangular laser elements were all oriented for light propagation along the N_g-axis (N_g-cut). This is because of two reasons. First, this crystal cut provides attractive thermo-optic properties (weak, positive and nearly spherical thermal lens [32]). Second, it gives access to the polarizations ***E*** || N_m and ***E*** || N_p corresponding to intense spectral bands both in absorption and emission [22]. The sample thickness (t) and aperture are listed in Table 1. Both input and output facets (N_m×N_p) were polished to laser quality and remained uncoated.

3. NEAR- AND MIR-INFRARED EMISSIONS

A. Stimulated-emission cross-sections

The stimulated-emission cross-sections for the $^3F_4 \rightarrow {}^3H_6$ transition (at ~1.9 μm) of Tm^{3+} ions in $KLu(WO_4)_2$ were reported before [31]. Here, we mainly focus on thulium emission originating from the $^3H_4$ state and suitable for laser operation, i.e., $^3H_4 \rightarrow {}^3F_4$ (at ~1.5 μm) and $^3H_4 \rightarrow {}^3H_5$ (at ~2.3 μm). We also briefly characterize the $^3F_4 \rightarrow {}^3H_6$ transition as it spectrally partially overlaps with the desired SWIR one.

First, polarized luminescence spectra $W_i(\lambda)$, where $i = p, m, g$ is the polarization index, were measured. As an excitation source, we used a Ti:Sapphire laser tuned to ~802 nm. The spectra at ~1.5 μm and ~1.9 μm were measured using an optical spectrum analyzer (OSA, AQ6375B, Yokogawa, spectral bandwidth, SBW = 1 nm). To measure the spectra at ~2.3 μm, we used a 0.6 m monochromator (HRS2, Jobin-Yvon, resolution: 4.5 nm), a lock-in amplifier (SR810 DSP, Stanford Research Systems) and an InSb photodetector (J10D series, Judson Infrared) cooled by liquid N_2. A Glan-Taylor polarizer was employed for polarized studies. The wavelength calibration was performed using an Hg lamp (Schwabe), and the response of the set-up was calibrated using a 20 W quartz iodine lamp so that the measured spectra $W_i(\lambda)$ could be calibrated for the spectral response of the set-up for the specific polarization yielding the calibrated spectra $W'_i(\lambda)$.

The stimulated-emission (SE) cross-sections, σ_{SE}, were calculated using the Füchtbauer–Ladenburg (F-L) formula [38]:

$$\sigma_{SE}^{i}(\lambda) = \frac{\lambda^5}{8\pi \langle n \rangle^2 \tau_{rad} c\,(1/3) \sum_{j=p,m,g} \int \lambda W'_j(\lambda) \mathrm{d}\lambda} \frac{W'_i(\lambda) B(JJ')}{}, \quad \textbf{(1)}$$

where λ is the light wavelength, $\langle n \rangle$ is the mean refractive index at the mean emission wavelength $\langle \lambda_{em} \rangle$, c is the speed of light, τ_{rad} is the radiative lifetime of the emitting state ($^3H_4$ or $^3F_4$), and B(JJ') is the luminescence branching ratio. We used the transition probabilities for Tm^{3+} determined by the Judd-Ofelt theory according to the intensity parameters Ω_2 = 9.01, Ω_4 = 1.36 and Ω_6 = 1.43 [10^{-20} cm^2], namely $\tau_{rad}(^3F_4)$ = 1.483 ms, $\tau_{rad}(^3H_4)$ = 0.203 ms and $B(^3H_4 \rightarrow {}^3F_4)$ = 7.86%, $B(^3H_4 \rightarrow {}^3H_5)$ = 3.29% [22]. The refractive indices were calculated from the Sellmeier equations [37]. The results are shown in Fig. 2.

The Tm:$KLu(WO_4)_2$ crystal exhibits a strong polarization anisotropy of the SE cross-sections for all the studied transitions. For the peak σ_{SE} values, the following relation is observed: $\sigma_{SE}(m) > \sigma_{SE}(p) > \sigma_{SE}(g)$. This anisotropy stems from the low symmetry of the rare-earth site in the $KLu(WO_4)_2$ host matrix (C_2). For each of the considered transitions, we calculated the wavelengths of all the possible purely electronic transitions between the Stark components of the involved multiplets using the reported crystal-field splitting [22]. They are shown as dashes in Fig. 2 and facilitate the assignment of the observed emissions.

For the $^3H_4 \rightarrow {}^3F_4$ transition, the emission band spans from 1.38 to 1.52 μm (according to the calculated electronic transitions) and the maximum σ_{SE} = 2.11×10^{-20} cm^2 at 1483 nm for the light polarization ***E*** || N_m.

For the $^3F_4 \rightarrow {}^3H_6$ transition, the emission band is much broader due to the relatively large total Stark splitting of the ground-state ($^3H_6$) and it spans from 1.67 to 1.95 μm (the electronic transitions), while the vibronic tail of the emission band extends beyond ~2 μm. The maximum σ_{SE} reaches 3.57×10^{-20} cm^2 at 1842 nm for ***E*** || N_m. The $^3F_4 \rightarrow {}^3H_6$ transition represents a quasi-three-level laser scheme with reabsorption. Thus, the laser emission is typically achieved at longer wavelengths. In particular, σ_{SE} = 0.91×10^{-20} cm^2 at 1946 nm for ***E*** || N_m. At this emission wavelength, the anisotropy of the SE cross-sections is expressed by the ratios $\sigma_{SE}(m) : \sigma_{SE}(p)$ = 3.7 and $\sigma_{SE}(m) : \sigma_{SE}(g)$ = 11. This imposes the emission to be linearly polarized in Tm:$KLu(WO_4)_2$ lasers. The determined σ_{SE} values agree with those calculated by the reciprocity method [31].

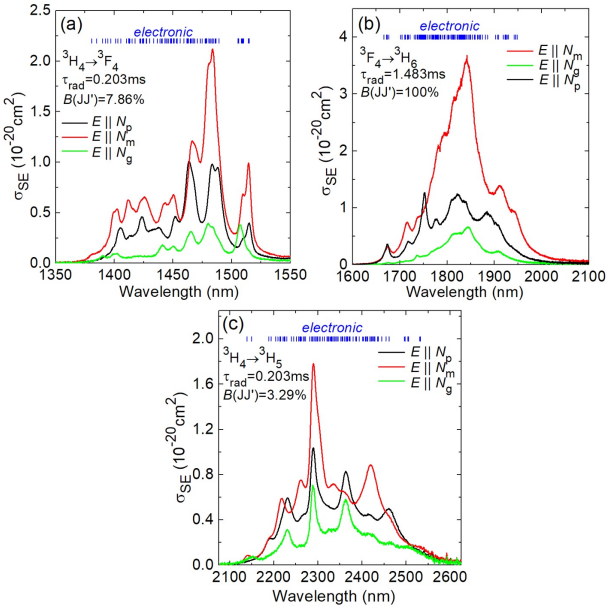

Fig. 2. Stimulated-emission (SE) cross-sections, σ_{SE}, for (a) $^3H_4 \rightarrow {}^3F_4$, (b) $^3F_4 \rightarrow {}^3H_6$ and (c) $^3H_4 \rightarrow {}^3H_5$ transitions of Tm^{3+} in monoclinic $KLu(WO_4)_2$ for light polarizations ***E*** || N_p, N_m and N_g, calculated using the F-L formula, Eq. (1). *Vertical dashes* indicate all possible purely electronic transitions between the Stark sub-levels of the involved multiplets.

Finally, for the transition of interest in this work, namely $^3H_4 \rightarrow {}^3H_5$, the emission band is also rather broad and spans from 2.14 to 2.53 μm (the electronic transitions). The laser wavelength for this quasi-four-level laser scheme is simply determined by the SE cross-section spectra. The maximum σ_{SE} is 1.78×10^{-20} cm^2 at 2289 nm and the corresponding emission bandwidth $\Delta\lambda_{em}$ (determined as the full width at its half maximum, FWHM), is 32.1 nm for ***E*** || N_m. The anisotropy of the SE cross-sections is weaker than for the $^3F_4 \rightarrow {}^3H_6$ transition, i.e., $\sigma_{SE}(m) : \sigma_{SE}(p)$ = 1.7 and $\sigma_{SE}(m) : \sigma_{SE}(g)$ = 2.5, however, it is enough to ensure natural selection of the laser polarization. The determined SE cross-section for the $^3H_4 \rightarrow {}^3H_5$ transition is higher than in any previously studied Tm^{3+}-doped fluoride or oxide crystal, and is assigned to the strong polarization-anisotropy of the optical properties in Tm:$KLu(WO_4)_2$, and in part – to the relatively short radiative lifetime of the emitting state ($^3H_4$). Indeed, for the most widespread crystal for ~2.3 μm lasers, Tm:$LiYF_4$, σ_{SE} reaches 0.57×10^{-20} cm^2 at 2305 nm and $\Delta\lambda_{em}$ is 25.8 nm for π-polarized light [25]. Considering the relatively broad emission band, Tm:$KLu(WO_4)_2$ appears to be attractive for mode-locked lasers at ~2.3 μm.

B. Vibronic contribution

As can be seen from Fig. 2(b),(c), the spectral ranges of purely electronic $^3F_4 \rightarrow {}^3H_6$ and $^3H_4 \rightarrow {}^3H_5$ transitions do not overlap. However, it is known that all Tm^{3+}-doped materials exhibit strong electron-phonon (vibronic) interaction leading to the broadening of their emission bands. For Tm^{3+}, this is determined by its location almost in the end of the lanthanide series [39,40]. Besides the broadening of the emission peaks corresponding to the particular Stark-to-Stark transitions, the electron-phonon coupling determines the shape of the vibronic tails of the emission bands corresponding to Stokes (S) and anti-Stokes (AS) processes [41]. The anti-Stokes vibronic tail is the one observed at wavelengths below the shortest wavelength of the pure electronic transition (occurring between the highest sub-level of the emitting multiplet and the lowest sub-level of the terminating one). The Stokes vibronic tail is observed at wavelengths above the longest wavelength of the pure electronic transition (occurring between the lowest sub-level of the emitting multiplet and the highest sub-level of the terminating one). The S vibronic tail of the $^3F_4 \rightarrow {}^3H_6$ transition and the AS one of the $^3H_4 \rightarrow {}^3H_5$ transition may overlap. This raises the question of attributing the emission occurring at intermediate wavelengths.

The analysis of the possible overlap of the $^3F_4 \rightarrow {}^3H_6$ and $^3H_4 \rightarrow {}^3H_5$ emissions of Tm^{3+} ions in $KLu(WO_4)_2$ is performed in Fig. 3 in terms of the SE cross-section spectra plotted in a semi-log scale. For the $^3F_4 \rightarrow {}^3H_6$ transition, the longest wavelength of the electronic transition is 1948 nm (occurring between the Stark sub-levels 5663 cm^{-1}($^3F_4$) and 530 cm^{-1}($^3H_6$) [21]). For the $^3H_4 \rightarrow {}^3H_5$ one, the shortest wavelength of the electronic transition is 2139 nm (occurring between the Stark sub-levels 12906 cm^{-1}($^3H_4$) and 8231 cm^{-1}($^3H_5$) [22]). The vibronic tails are well fitted with the exponential law [42]:

$$\sigma_S = \sigma_0 \exp(-\alpha_S \Delta E), \quad \textbf{(2a)}$$

$$\sigma_{AS} = \sigma_0 \exp(-\alpha_{AS} \Delta E), \quad \textbf{(2b)}$$

where ΔE is the energy mismatch between the vibronic and the electronic transition, σ_0 is the transition cross-section at the photon energy corresponding to the electronic transition and the factors α_S and α_{AS} depend on the host material. For $Tm:KLu(WO_4)_2$, we obtain the material-dependent factors α_S = 10.0±0.7×10^{-3} cm^{-1} and α_{AS} = 14.5±1.5×10^{-3} cm^{-1}. The wavelength at which the SE cross-sections for both transitions are equal, is λ_{eq} = 2104±10 nm.

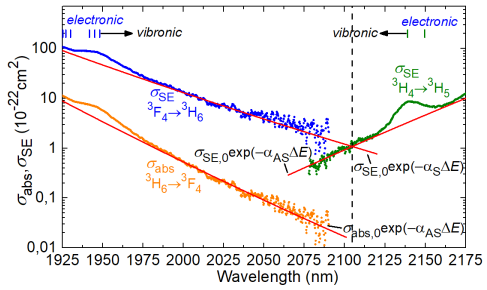

Fig. 3. Electron-phonon coupling bridges the gap between the $^3F_4 \rightarrow {}^3H_6$ and $^3H_4 \rightarrow {}^3H_5$ electronic transitions of Tm^{3+} in monoclinic $KLu(WO_4)_2$ crystal: a semi-logarithmic plot of the stimulated-emission, σ_{SE}, and absorption, σ_{abs}, cross-sections for the $^3F_4 \leftrightarrow {}^3H_6$ and $^3H_4 \rightarrow {}^3H_5$ transitions for light polarization $\boldsymbol{E} \parallel N_m$. *Symbols* – experimental data, *lines* – exponential fits to the phonon sidebands of the spectral bands, Eq. (2). *Vertical dashes* indicate the purely electronic transitions between the Stark sub-levels of the involved multiplets. *Black vertical dashed line* indicates the wavelength of equal σ_{SE} for the two transitions.

Thus, the gap between the $^3F_4 \rightarrow {}^3H_6$ and $^3H_4 \rightarrow {}^3H_5$ electronic transitions of Tm^{3+} in $KLu(WO_4)_2$ is bridged by vibronic transitions. The performed analysis allowed us to propose a criterion for the attribution of emissions within this gap. All the emissions with wavelengths exceeding λ_{eq} will be assigned as such related to the $^3H_4 \rightarrow {}^3H_5$ transition (either of electronic or vibronic nature), and all the emissions at shorter wavelengths – to the $^3F_4 \rightarrow {}^3H_6$ one.

Let us discuss previously obtained results on $Tm:KLu(WO_4)_2$ lasers in light of this criterion. Typically, bulk lasers based on this crystal operated at a wavelength of ~1.94 μm, e.g., Serres *et al.* reported on a diode-pumped 3 at.% Tm doped laser delivering multi-watt output at 1946 nm [32]. This wavelength is close to the longest wavelength of the $^3F_4 \rightarrow {}^3H_6$ purely electronic transition.

Longer wavelengths were achieved under two circumstances. First, highly-doped crystals provided emission above 2 μm using low output coupling and without any spectrally-selective elements: Mateos *et al.* reported a 0.59 W output power at 2005-2045 nm with a slope efficiency of 51% for 15 at.% Tm doping [43]. Such wavelengths clearly represent vibronic emission. This behavior was mainly induced by the high Tm^{3+} doping concentration as lower inversion ratio was needed to ensure the gain needed to compensate for the losses. For small inversion ratios, the gain spectra for the quasi-three-level $^3F_4 \rightarrow {}^3H_6$ transition are flat and broad extending beyond 2 μm.

Second, long laser wavelengths were achieved in bulk Tm lasers employing a spectrally-selective output coupler providing high transmission at <2 μm: Loiko *et al.* reported on a diode-pumped 3 at.% $Tm:KLu(WO_4)_2$ laser delivering 1.17 W with a slope efficiency of 39% at 2109-2133 nm [44], the longest wavelength achieved so far with this material. Besides the assignment of this emission to the vibronic mechanism, the authors suggested a resonant mechanism involving low-frequency Raman modes of the host matrix (a possible contribution of CW self-Raman conversion). Note that the use of a similar cavity mirror allowed the authors in [34] to operate a ML $Tm:KLu(WO_4)_2$ laser above 2 μm (at 2037 nm) avoiding the unwanted structured water vapor atmospheric absorption and achieving fs pulse duration.

According to the proposed criterion, the emission at 2109-2133 nm observed in [44] can be in part assigned to the $^3H_4 \rightarrow {}^3H_5$ transition (the vibronic contribution). Probably because of the limited reflection band of the cavity mirrors in [44], the authors were unable to achieve laser emission at longer wavelengths corresponding to the electronic $^3H_4 \rightarrow {}^3H_5$ transition.

C. Lifetime of the $^3H_4$ multiplet: An overview

The luminescence dynamics for Tm^{3+} ions in $KLu(WO_4)_2$ was studied previously. In this Section, we aim to summarize the reported results and to analyze them concerning the targeted $^3H_4 \rightarrow {}^3H_5$ transition, i.e., by focusing on the $^3H_4$ multiplet. The intrinsic lifetime τ_{30} determined in the limit of a very low Tm concentration (thus not being affected by the CR and energy-migration) is in general shorter than the radiative one because of the multi-phonon NR relaxation [45,46]:

$$\frac{1}{\tau_{30}} = \frac{1}{\tau_{3rad}} + W_{NR}, \quad \textbf{(3a)}$$

$$W_{NR} = Ce^{-\alpha \Delta E}, \quad \textbf{(3b)}$$

where W_{NR} is the rate constant (expressed in [s^{-1}]) of the multi-phonon NR relaxation which depends on the energy-gap to the lower-lying state ΔE and the maximum phonon energy $h\nu_{ph}$, and C and α are characteristic constants for the material. C has the meaning of a NR rate constant in the limit of zero energy gap ($\Delta E \rightarrow 0$), and $\alpha = -\ln(\varepsilon)/(h\nu_{ph})$, where ε is the ratio between the probabilities of m-phonon and m – 1-phonon relaxation.

In Fig. 4(a), we analyzed the W_{NR} values calculated by comparing the radiative and intrinsic lifetimes of various excited-states of several rare-earth ions in several $KRE(WO_4)_2$ crystals [22,47-49] considering their

very close phonon spectra. The experimental data on W_{NR} are well fitted with Eq. (3b) yielding the following best-fit material parameters: C = 2.14±2×10^8 s^{-1} and α = 2.90±0.1×10^{-3} cm. These parameters reasonably agree with those estimated by de Mendivil *et al.* [47].

Regarding the $^3H_4$ Tm^{3+} state, according to the Judd-Ofelt analysis by Silvestre *et al.* [22], the radiative lifetime τ_{3rad} = 0.203 ms. This obviously contradicts the luminescence lifetime measured by the same authors for low doped sample (0.5 at.% Tm), τ_{3lum} = 0.230 ms [22] which can be approximately taken as the intrinsic one. The application of Eq. (3b) with the material parameters determined above yields W_{NR} = 2.2±1×10^3 s^{-1} and, accordingly, τ_{3rad} about 0.47 ms. The difference between this value and the one obtained from the Judd-Ofelt calculations can be explained by the error in the latter. At the moment, we are unable to clarify this discrepancy and further analysis is needed (e.g., by employing the modified Judd-Ofelt theory accounting for the configuration interaction).

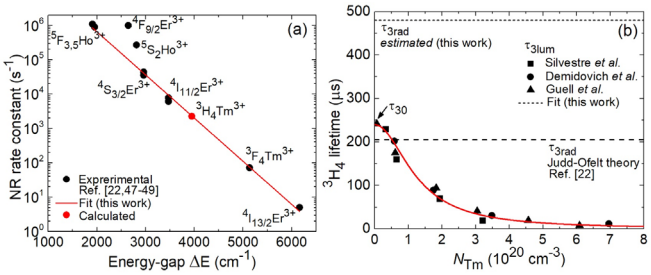

Fig. 4. (a) The rate constants of multi-phonon non-radiative relaxation W_{NR} versus the energy-gap to the lower-lying state ΔE for various excited-states of rare-earth ions in monoclinic double tungstate crystals: *circles* – data from [22,47-49], *red line* – fit using Eq. (3b), *red circle* – estimation for the $^3H_4$ Tm^{3+} state; (b) Luminescence lifetimes of the $^3H_4$ Tm^{3+} state in monoclinic double tungstate crystals: *symbols* – data from [22,50,51], *red curve* – fit using Eq. (4a), horizontal *dashed lines* – estimations of the radiative lifetime (this work and Ref. [22]).

The luminescence lifetime of the $^3H_4$ state can be represented as a function of the Tm doping concentration (neglecting the energy-migration) [17,52]:

$$\frac{1}{\tau_{3lum}} = \frac{1}{\tau_{30}} + W_{CR}. \quad \textbf{(4a)}$$

$$W_{CR} = C_{CR} N_{Tm}^2. \quad \textbf{(4b)}$$

Here, W_{CR} is the CR rate constant (expressed in [s^{-1}]) and C_{CR} is the concentration-independent CR parameter (expressed in [cm^{6}s^{-1}]). In Fig. 4(b), we summarize the luminescence lifetimes of the $^3H_4$ multiplet of Tm^{3+} ions reported for $KLu(WO_4)_2$ and its isomorph crystals [22,50,51]. In this analysis, we accounted for the different cation density per 1 at.% doping in different crystals. As can be seen, for different host-forming cations in the monoclinic double tungstate crystals, the $^3H_4$ lifetime of the dopant ones (Tm^{3+}) follows nearly the same trend. The fitting of the experimental data using Eq. (4) yields the following parameters: τ_{30} = 0.24±0.01 ms and C_{CR} = 2.70±0.15×10^{-37} cm^{6}s^{-1}. These values are in reasonable agreement with those published in [17].

The use of Eq. (4a) with the determined best-fit τ_{30} and C_{CR} parameters yields τ_{3lum} = 222, 130 and 50 μs for the 0.5, 1.5 and 3.0 at.% Tm^{3+}-doped $KLu(WO_4)_2$ crystals, respectively.

4. LASER PERFORMANCE

A. Laser set-up

The scheme of the laser set-up is shown in Fig. 5(a). A simple linear nearly-hemispherical cavity was used. It comprised a flat pump mirror (PM) coated for high transmission (HT, T = 95.3%) at 0.77-0.81 μm and for high reflection (HR, R > 99.9%) at 2.12–2.50 μm, and a set of concave output couplers (OCs) all having the same radii of curvature (RoC) of 100 mm and a measured transmission T_{OC} at 2.18–2.35 μm of 0.1% (±0.05%), 0.7%, 1.3% or 4.0% (±0.2%). The OCs, except the 0.1% one, provided high reflectivity (R > 97%) at the pump wavelength. In order to suppress the unwanted $^3F_4 \rightarrow {}^3H_6$ transition, all the OCs provided HT (T > 90%) at 1.80-1.98 μm. Note that no special requirements were applied for the PM and its reflectivity at ~1.95 μm was R ~ 93%. The total geometrical cavity length was ~100 mm.

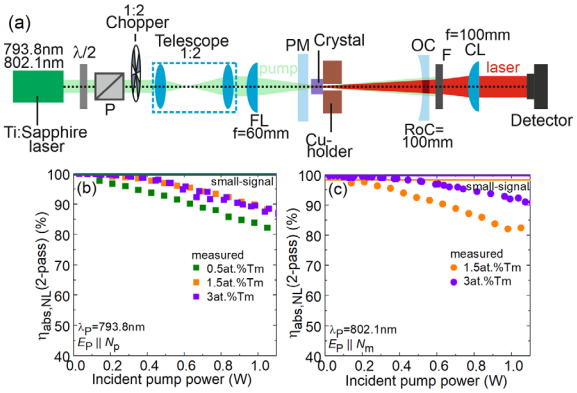

Fig. 5. (a) Scheme of the Tm laser operating on the $^3H_4 \rightarrow {}^3H_5$ transition: λ/2 –half-wave plate, P – Glan-Taylor polarizer, FL and CL – focusing and collimating lenses, respectively, PM – pump mirror, OC – output coupler, F – bandpass filter; (b,c) total (double-pass) pump absorption under non-lasing conditions $\eta_{abs,NL(2\text{-pass})}$ for the studied laser crystals. The pump polarization is (b) $\boldsymbol{E_P} \parallel N_p$ and (c) $\boldsymbol{E_P} \parallel N_m$.

Three laser crystals with Tm doping levels of 0.5, 1.5 and 3.0 at.% were employed, see Table 1. All of them were N_g-cut. The crystals were mounted on a massive passively-cooled Cu-holder using a silver thermal paste for better heat removal. The laser crystals were placed close to the PM leaving only a small air gap (less than 1 mm).

As a pump source, we employed a CW Ti:Sapphire laser (3900S, Spectra Physics) delivering up to 3.6 W at the wavelengths of 770-810 nm (tunable output) in the fundamental mode ($M^2 \approx 1$). The pump wavelength thus corresponded to the $^3H_6 \rightarrow {}^3H_4$ Tm^{3+} transition. The incident pump power was adjusted using a half-wave plate and a Glan-Taylor polarizer oriented in such a way that the pump polarization corresponded to $\boldsymbol{E_P} \parallel N_p$ or $\boldsymbol{E_P} \parallel N_m$ in the crystal. The pump beam was expanded using a home-made telescope (reimaging ratio: 1:2) and focused into the crystal using an achromatic lens (focal length: f = 60 mm). A mechanical chopper (frequency: 20 Hz, duty cycle: 1:2) was introduced in the beam path to ensure quasi-CW pumping reducing the heat loading in the crystal. The pump spot radius in the focus w_P was 40±10 μm (at the 1/e^2 level, as measured by the optical knife method) and the calculated confocal parameter of the pump beam $2z_R$ exceeded 10 mm (in the crystal). The radius of the laser mode in the crystal was calculated by the ABCD-method accounting for the positive thermal lens to be w_L = 40-44±5 μm (slowly decreasing with the pump power). Thus, relatively good mode-matching was observed.

For each crystal, first, we measured pump absorption under non-lasing (NL) conditions in a single-pass. The measurements were done for the pump wavelengths of 793.8 and 802.1 nm corresponding to the polarizations $\boldsymbol{E_P} \parallel N_p$ or $\boldsymbol{E_P} \parallel N_m$, respectively. Then, the second pass of the pump was taken into account leading to the total value $\eta_{abs,NL(2\text{-pass})}$ (it does not include Fresnel losses at the uncoated crystal surfaces). The decreasing $\eta_{abs,NL(2\text{-pass})}$ value with the incident pump power, as shown

in Fig. 5(b,c), represents the effect of ground-state bleaching (absorption saturation). The absorption under lasing (L) conditions was estimated from the $\eta_{abs,NL(2\text{-pass})}$ value for each OC at the threshold pump power.

To separate the $^3H_4 \rightarrow {}^3H_5$ laser emission from the residual (non-absorbed) pump, we used a bandpass filter (FB2250-500, Thorlabs). The spectra of the laser emission were measured using an optical spectrum analyzer (OSA, AQ6375B, Yokogawa, resolution: 0.2 nm). The pump wavelength was determined using another OSA (Ando AQ6315-E, resolution: 0.1 nm). The laser beam profile in the far-field was captured using a pyroelectric camera (PY-III-HR-C-A, Ophir). The beam quality factors M^2_{xy} were measured by an ISO-standard method using a single spherical CaF_2 lens (f = 100 mm) placed after the OC.

In addition to the laser experiment on the $^3H_4 \rightarrow {}^3H_5$ transition, we studied the performance of the 3.0 at.% Tm doped crystal on the $^3F_4 \rightarrow {}^3H_6$ transition. For this, the same set-up was used, only the cavity mirrors were replaced. The flat PM provided HT (T = 97.4%) at ~0.79 μm and HR at 1.87-2.30 μm and the concave OCs (RoC = -100 mm) provided T_{OC} of 0.5%-15% at 1.90-2.08 μm. The OCs provided relatively high transmission of T >70% at the pump wavelength, so that the pumping was in a single-pass in this case.

B. The $^3H_4 \rightarrow {}^3H_5$ transition: Best-performing crystal

At first, we report the results achieved with the best-performing crystal (3 at.% Tm doping), the optimum pump polarization ($\boldsymbol{E}_P \parallel N_p$) and the corresponding pump wavelength λ_P of 793.8 nm. We will specify the peak output power obtained by multiplying the average output power by a factor of ×2. This factor was confirmed in experiments in true CW regime performed at low pump powers. For the specified pump conditions, the pump absorption under lasing conditions $\eta_{abs,L(2\text{-pass})}$ decreased with the output coupling from 96.9% (T_{OC} = 0.1%) to 89.4% (T_{OC} = 4%). For all OCs, no colasing at wavelengths below 2 μm (the $^3F_4 \rightarrow {}^3H_6$ electronic transition) was observed, verified by spectral measurements in the 1.7 – 2.4 μm range.

The power characteristics of the laser are shown in Fig. 6. It generated a maximum peak output power of 1.12 W at ~2.22 and 2.29 μm (multi-color emission) with a slope efficiency η of 69.2% (determined with respect to the absorbed pump power P_{abs}). The laser threshold was at P_{th} = 0.45 W and the optical-to-optical efficiency, calculated with respect to the pump power incident on the crystal, η_{opt}, reached 44.4% (all characteristics are specified for T_{OC} = 1.3%). The laser threshold gradually increased with T_{OC}, from 0.28 W for the 0.1% OC up to 0.58 W for the 4% OC. The input-output dependences were nonlinear near the laser threshold. No thermal roll-over or fracture of the crystal was observed up to at least P_{abs} ~ 2 W.

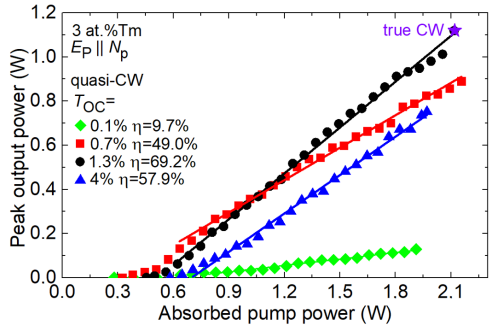

Fig. 6. Input-output dependences for the Tm laser pumped at 793.8 nm ($\boldsymbol{E}_P \parallel N_p$) and operating on the $^3H_4 \rightarrow {}^3H_5$ transition in the quasi-CW mode (duty cycle: 1:2); η – slope efficiency. Tm doping: 3 at.%. The *asterisk* indicates the maximum power obtained in true CW regime (T_{OC} = 1.3%).

The true CW laser performance was studied only for the optimum T_{OC} of 1.3%. The input-output dependence was almost identical to that for quasi-CW pumping indicating relatively weak thermal effects for the particular Tm doping level (3 at.% Tm) and output coupling. For the maximum available absorbed pump power P_{abs} of 2.12 W, the CW output power amounted to 1.12 W, as shown by asterisk in Fig. 6.

The laser generated a linearly polarized output ($\boldsymbol{E} \parallel N_m$) with a polarization degree P exceeding 99%. The polarization state was naturally selected by the anisotropy of the gain in agreement with the SE cross-section spectra, cf. Fig. 2(c). The laser emission spectra were dependent both on the output coupling and the pump power, Fig. 7. At low pump powers near the threshold, the laser operated at ~2.29 μm for all the studied OCs. This corresponds to the main maximum in the SE cross-section spectra of Tm:$KLu(WO_4)_2$. This laser line was maintained with increasing pump power only for the highest studied output coupling (T_{OC} = 4%). For lower T_{OC}, other emission lines appeared at shorter wavelengths (2.14 – 2.22 μm). A similar behavior was recently observed in another oxide laser crystal - Tm:$Y_3Al_5O_{12}$ [29].

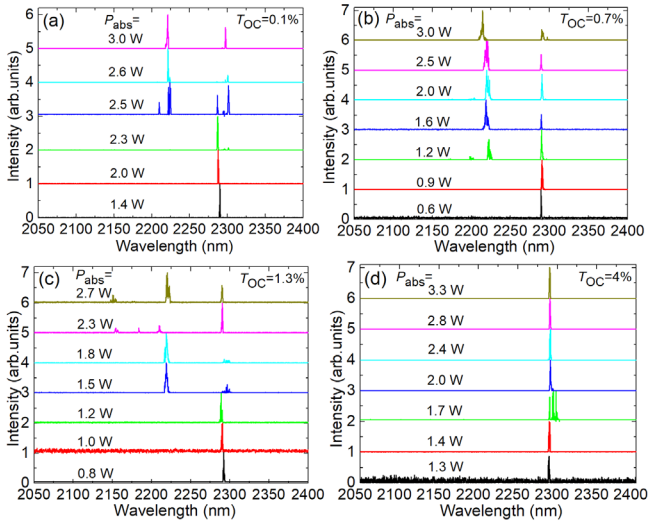

Fig. 7. The emission spectra from the thulium laser (3 at.% Tm) operating on the $^3H_4 \rightarrow {}^3H_5$ transition at different absorbed pump powers P_{abs}. Output coupling: (a) 0.1%, (b) 0.7%, (c) 1.3% and (d) 4.0%. The laser polarization is $\boldsymbol{E} \parallel N_m$.

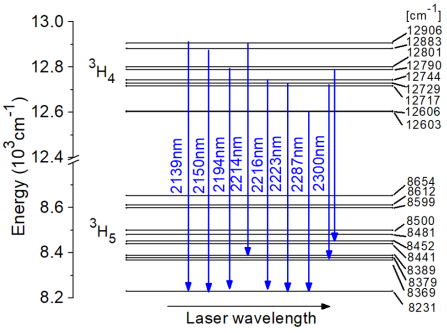

Fig. 8. Crystal-field splitting of the $^3H_4$ and $^3H_5$ multiplets of Tm^{3+} in $KLu(WO_4)_2$ crystal (after [22]) and the assignment of the observed laser transitions.

As pointed out above, the assignment of Tm^{3+} emissions at the intermediate wavelengths of 2.0-2.2 μm may be complicated due to the partial overlap of the $^3F_4 \rightarrow {}^3H_6$ and $^3H_4 \rightarrow {}^3H_5$ emission bands. The first step is to assign the laser lines to electronic transitions. This was

possible for all the observed emission wavelengths assuming transitions between the Stark components of the $^3H_4$ and $^3H_5$ multiplets, as shown in Fig. 8 where the transitions are sorted out in the order of increasing wavelength (2139, 2150, 2194, 2214, 2216, 2223, 2287 and 2300 nm). All these emission wavelengths are longer than the λ_{eq} one (2104 nm) defined in Section 3B. Thus, the observed laser emission can be unambiguously assigned to the $^3H_4 \rightarrow {}^3H_5$ transition. Now let us discuss the physical reasons for the multi-color emission at low output couplings. Note that our OCs were supporting laser operation at 2.18–2.35 μm. One reason is the highly probable etalon effect at the PM / crystal interface. This was verified by varying the pump power which, due to the positive thermal expansion of the crystal in the longitudinal direction, affected the laser spectrum. Another possible reason is the additional gain arising from the vibronic tail of the $^3F_4 \rightarrow {}^3H_6$ transition. At such wavelengths, the reabsorption losses are almost negligible. Note that for any Tm laser operating on the $^3H_4 \rightarrow {}^3H_5$ transition, a notable fraction of ions is accumulated in the metastable intermediate state ($^3F_4$). If no special attention is paid to suppress the emission at ~1.9 μm, colasing at ~1.9 μm and 2.3 μm will be observed. In our case, the spectral component below 2 μm is suppressed by the appropriate coatings of the OCs. The third reason is the resonant electron-phonon coupling with the low-frequency Raman modes of the host matrix [44].

The mode profile of the Tm laser in the far-field is shown Fig. 9(a). The output beam was nearly circular which agrees with the weak astigmatism of the thermal lens in N_g-cut Tm:KLu(WO$_4$)$_2$ [32]. The 1D intensity profiles in the horizontal (x, || N_m) and vertical (y, || N_p) directions were fitted with a Gaussian distribution revealing weak mode wings and probably slightly multimode behavior. To clarify that, the beam quality factors $M^2_{x,y}$ were evaluated as shown in Fig. 9(b). They amounted to 2.2±0.1 and 2.6±0.1, respectively. Thus, despite the high beam quality of the pump radiation ($M^2 \approx 1$), the Tm laser generated a slightly multimode output. We attribute this to two reasons: (i) quasi-four-level nature of the $^3H_4 \rightarrow {}^3H_5$ transition with no reabsorption and (ii) strong positive (focusing) thermal lens in the Tm:KLu(WO$_4$)$_2$ crystal. As the thermal lens is pump-dependent, with increasing the pump power, the size of the fundamental mode in the crystal is decreased with respect to the pump spot size and higher-order modes are supported. Note that for Tm:KLu(WO$_4$)$_2$ lasers operating on the $^3F_4 \rightarrow {}^3H_6$ transition, an additional mode filtering is provided by reabsorption losses in the wings of the higher-order modes spatially overlapping with unpumped regions of the crystal [17]. This is however not the case for the quasi-four level $^3H_4 \rightarrow {}^3H_5$ lasing. The possible reabsorption arising from the vibronic sideband of the $^3H_6 \rightarrow {}^3F_4$ transition is very weak and exponentially decreases with the wavelength, cf. Fig. 3.

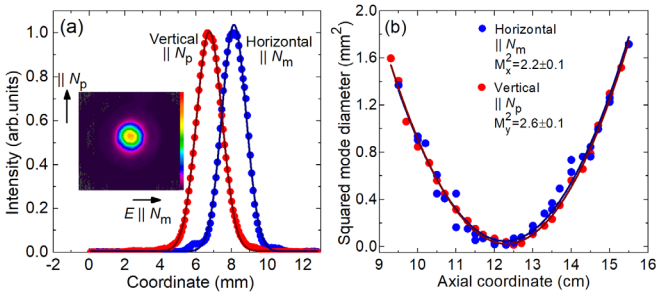

Fig. 9. Spatial characteristics of the output of the Tm laser operating on the $^3H_4 \rightarrow {}^3H_5$ transition: (a) 1D intensity profiles in the horizontal (x, || N_m) and vertical (y, || N_p) directions: *symbols* – experimental data, *curves* – Gaussian fits, *inset* – 2D mode profile in the far-field; (b) evaluation of the beam quality factors $M^2_{x,y}$. Tm doping: 3 at.%. T_{OC} = 1.3%, P_{abs} = 0.8 W. The laser polarization ($\boldsymbol{E}$ || N_m) is horizontal.

C. The $^3F_4 \rightarrow {}^3H_6$ transition: A comparison

CW laser operation of Tm:KLu(WO$_4$)$_2$ crystal on the $^3F_4 \rightarrow {}^3H_6$ transition was addressed before [31,32]. Here, we studied this laser channel only to provide a direct comparison with the targeted $^3H_4 \rightarrow {}^3H_5$ transition (such a comparison is performed for the first time).

We implemented the same 3 at.% Tm:KLu(WO$_4$)$_2$ crystal in a similar cavity with the mirrors coated to support the emission at ~1.9 μm. The results are shown in Fig. 10(a,b). The laser generated a maximum output peak power of 0.95 W at 1942-1950 nm with a slope efficiency of 49.8%. The laser threshold was at P_{th} = 0.13 W and η_{opt} was 38.9% (for T_{OC} = 10%). The laser threshold increased with the output coupling, from 0.05 W for T_{OC} = 0.5% up to 0.19 W for T_{OC} = 15%. The input-output dependences were close to linear. The laser output was linearly polarized ($\boldsymbol{E}$ || N_m) and the spectra were weakly dependent on the pump power. With increasing output coupling, the emission wavelength experienced a slight blue-shift, from 1954-1992 nm for T_{OC} = 0.5% to 1941-1946 nm for T_{OC} = 15%. This behavior is well-known for quasi-three-level Tm lasers and is related to decreasing reabsorption losses at higher inversion in the gain medium associated with higher T_{OC}. Even without spectrally-selective mirrors, we were able to observe vibronic emissions for the lowest output coupling (wavelengths above 1948 nm, see Section 3B).

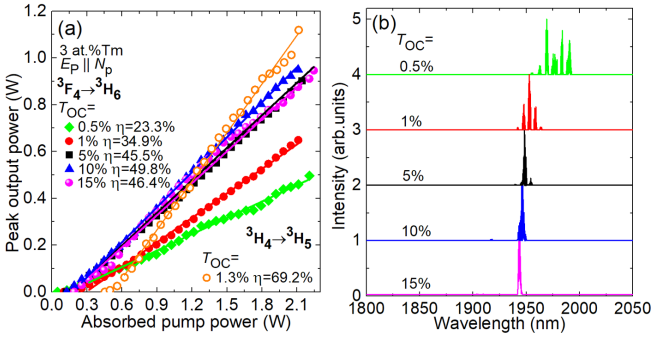

Fig. 10. Tm laser pumped at 793.8 nm ($\boldsymbol{E}_P$ || N_p) and operating on the $^3F_4 \rightarrow {}^3H_6$ transition in quasi CW mode (duty cycle: 1:2): (a) input-output dependences, η – slope efficiency; the output dependence for the laser operating on the $^3H_4 \rightarrow {}^3H_5$ transition is given for comparison; (b) typical laser emission spectra measured at P_{abs} = 0.5 W. The laser polarization is $\boldsymbol{E}$ || N_m. Tm doping: 3 at.%.

Previously, a compact (microchip-type) CW 3 at.% Tm:KLu(WO$_4$)$_2$ laser generated 3.2 W at 1946 nm with a slope efficiency of 50.4% [32]. Better power scaling capabilities as compared to the present work are mainly due to the use of diode-pumping and active (water) cooling of the laser crystal.

In Fig. 10(a), we directly compare the 3 at.% Tm:KLu(WO$_4$)$_2$ lasers operating on the $^3F_4 \rightarrow {}^3H_6$ and $^3H_4 \rightarrow {}^3H_5$ transitions (for the best OC). Surprisingly, the laser operating on the latter transition provides higher peak output power and slope efficiency albeit at greatly increased laser threshold. The difference in P_{th} is mainly due to the great difference in the intrinsic lifetimes of the upper laser levels, $\tau_{30}(^3H_4)$ = 0.24 ms (this work) and $\tau_{10}(^3F_4)$ = 1.34 ms [31].

The slope efficiency of Tm lasers operating on the $^3F_4 \rightarrow {}^3H_6$ transition is primarily governed by the pump quantum efficiency η_{q1} indicating the number of excitations to the upper laser level ($^3F_4$) per number of absorbed pump photons at ~0.8 μm. This parameter depends on the Tm doping level due to the cross-relaxation (CR) process, $^3H_4(Tm_1) + {}^3H_6(Tm_2) \rightarrow {}^3F_4(Tm_1) + {}^3F_4(Tm_2)$ [17,52]:

$$\eta_{q1} = 1 + \frac{W_{CR}}{(1/\tau_{30}) + W_{CR}}. \quad (5)$$

Here, W_{CR} is the CR rate constant defined by Eq. (4b) and C_{CR} is the concentration-independent CR parameter. For high Tm doping, efficient CR may result in η_{q1} approaching 2 (two-for-one pump process). Thus, the laser slope efficiency may exceed the Stokes limit under lasing conditions setting the upper limit of $\eta < 2\eta_{StL}$, where $\eta_{StL} = \lambda_P/\lambda_L$ and λ_P and λ_L are the pump and laser wavelengths, respectively. Indeed, very high η_{q1} value of 1.98±0.02 was observed in a highly-doped 15 at.% Tm:$KLu(WO_4)_2$ laser emitting at ~1.9 μm [43]. For the case of 3 at.% Tm doping, Eq. (5) yields η_{q1} = 1.79 which also explains the high slope efficiency observed in the present work.

For the 3 at.% Tm-doped crystal, the round-trip passive cavity losses were estimated from the Caird analysis [53] to be L = 0.58±0.2%.

The higher slope efficiency for the laser operating on the $^3H_4 \rightarrow {}^3H_5$ transition is due to another energy-transfer process, namely energy-transfer upconversion, see Section 4E.

D. The $^3H_4 \rightarrow {}^3H_5$ transition: Effect of pump polarization

The strong anisotropy of the spectroscopic properties of Tm:$KLu(WO_4)_2$ allows one to select the pump polarization along different principal optical directions. In Fig. 11, we compare the performance of the same crystal (1.5 at.% Tm doped) pumped with $\boldsymbol{E_P} \parallel N_p$ and $\boldsymbol{E_P} \parallel N_m$ polarizations. Note the difference in the corresponding pump wavelengths, 793.8 nm and 802.1 nm, respectively, corresponding to different local peaks in the absorption spectra. Physically, this difference arises from different polarization selection rules for light polarized along the C_2 symmetry axis ($\parallel N_p$) and for light polarizations lying in the mirror plane ($\perp C_2$, $\parallel N_m$) of the monoclinic $KLu(WO_4)_2$ crystal. Pumping in $\boldsymbol{E_P} \parallel N_p$ gives access to much higher peak absorption cross-sections σ_{abs} = 10.0×10^{-20} cm^2 whilst smaller absorption bandwidth $\Delta\lambda_{abs}$ = 1.6 nm, as compared to pumping in $\boldsymbol{E_P} \parallel N_m$ (σ_{abs} = 5.95×10^{-20} cm^2 and $\Delta\lambda_{abs}$ = 4.0 nm) [31].

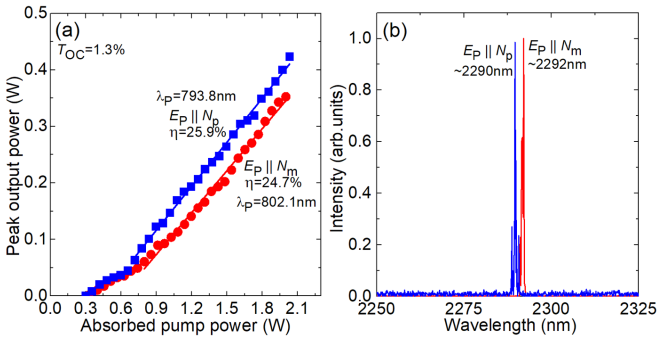

Fig. 11. Effect of the pump polarization ($\boldsymbol{E_P} \parallel N_m$ and $\boldsymbol{E_P} \parallel N_p$) on (a) $^3H_4 \rightarrow {}^3H_5$ laser performance, η – slope efficiency and (b) laser emission spectra captured at P_{abs} = 1.1 W for 1.5 at.% Tm:$KLu(WO_4)_2$. Quasi-CW operation (duty cycle: 1:2). The laser polarization is $\boldsymbol{E} \parallel N_m$.

Slightly better laser performance was observed for pumping with $\boldsymbol{E_P} \parallel N_p$: the laser generated 0.42 W at ~2290 nm with η = 25.9% and a laser threshold of P_{th} = 0.30 W. For the second studied pump polarization, the laser threshold slightly increased to P_{th} = 0.32 W and the output dependence was more nonlinear above it. This led to lower output power (0.35 W) at ~2292 nm. However, the slope efficiency was almost unchanged (η = 24.7%). All the characteristics are specified for T_{OC} = 1.3%. The pump absorption when pumping in $\boldsymbol{E_P} \parallel N_p$ was slightly higher. The total (double-pass) pump absorption at the threshold pump power $\eta_{abs,L(2\text{-pass})}$ for T_{OC} = 1.3% was calculated to be 96.2% and 92.3% for $\boldsymbol{E_P} \parallel N_p$ and $\boldsymbol{E_P} \parallel N_m$, respectively.

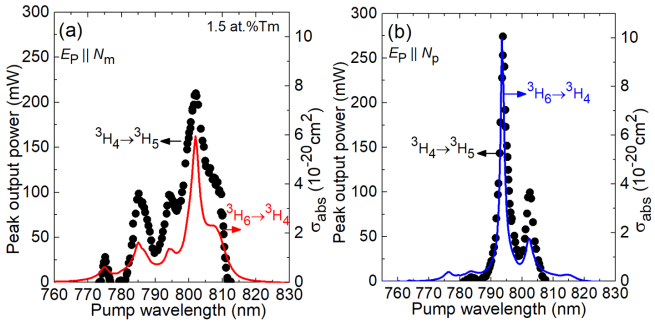

Fig. 12. Laser excitation spectra (output power *vs.* pump wavelength) for the Tm laser operating on the $^3H_4 \rightarrow {}^3H_5$ transition for pump polarization (a) $\boldsymbol{E_P} \parallel N_m$ and (b) $\boldsymbol{E_P} \parallel N_p$. The absorption cross-sections, σ_{abs}, for the $^3H_6 \rightarrow {}^3H_4$ Tm^{3+} transition are shown for comparison. Quasi-CW operation (duty cycle: 1:2). P_{inc} = 1.8 W. Tm doping: 1.5 at.%.

In Fig. 12, we present the laser excitation spectra for the 1.5 at.% Tm:$KLu(WO_4)_2$ pumped in two polarizations, $\boldsymbol{E_P} \parallel N_p$ and $\boldsymbol{E_P} \parallel N_m$, i.e. plots of the (peak) output power vs. the pump wavelength λ_P. The incident pump power was fixed to P_{inc} = 1.8 W and it was weakly dependent (within a measurement error of ±5%) on λ_P in the 770-820 nm spectral range. The coatings of the PM and OC exhibited flat spectral profiles at these wavelengths. Independent of the pump polarization, the laser polarization was naturally selected to be $\boldsymbol{E} \parallel N_m$. In Fig. 12, for comparison, we also show the polarized absorption cross-section spectra for the $^3H_6 \rightarrow {}^3H_4$ Tm^{3+} transition. For $\boldsymbol{E_P} \parallel N_p$, laser emission was observed when varying the pump wavelength in the 781.2-807.6 nm range and for $\boldsymbol{E_P} \parallel N_m$ – in the 773.1-812.7 nm range. The shape of the laser excitation spectra matched well that of the polarized absorption spectra.

E. The $^3H_4 \rightarrow {}^3H_5$ transition: Effect of the doping concentration

A summary of the laser experiments on the $^3H_4 \rightarrow {}^3H_5$ Tm^{3+} transition with the 0.5, 1.5 and 3.0 at.% Tm^{3+}-doped crystals performed with polarized pump ($\boldsymbol{E_P} \parallel N_p$ and $\boldsymbol{E_P} \parallel N_m$) is presented in Table 2. The input-output dependences measured using the same output coupling (T_{OC} = 1.3%) and pump polarization ($\boldsymbol{E_P} \parallel N_p$) are compared in Fig. 13(a). With increasing the Tm doping concentration, the slope efficiency of the laser η greatly increased from 10.7% (0.5 at.% Tm) to 69.2% (3.0 at.% Tm), so that the maximum slope efficiency well exceeded the Stokes limit, η_{StL} = 35.8%. Let us discuss this behavior.

Table 2. Output Characteristics[a] of Thulium Lasers at ~2.3 μm

Tm, at.%	λ_P, nm	P_{out}, W	η, %	P_{th}, W	λ_L, nm	η_{opt}, %
0.5	793.8 (N_p)	0.17	10.7	**0.28**	2290-2293	6.9
1.5	793.8 (N_p)	0.42	25.9	0.30	2288-2290	17.6
	802.1 (N_m)	0.35	24.7	0.32	2291-2292	14.4
3.0	793.8 (N_p)	**1.12**	**69.2**	0.45	2218-2223, 2290-2294	**44.4**
	802.1 (N_m)	1.02	67.7	0.44	2214-2219, 2289-2293	40.5

[a] λ_P – pump wavelength (polarization given in brackets), P_{out} – peak output power, P_{th} – laser threshold, η – slope efficiency *vs.* P_{abs}, λ_L – laser wavelength, η_{opt} – optical-to-optical efficiency. T_{OC} = 1.3%.

Recently, we developed a model describing Tm lasers operating on the $^3H_4 \rightarrow {}^3H_5$ transition [25]. It is based on accounting for two key energy-transfer processes affecting the population of the upper laser level ($^3H_4$), namely the CR, $^3H_4(Tm_1) + {}^3H_6(Tm_2) \rightarrow {}^3F_4(Tm_1) + {}^3F_4(Tm_2)$, and the reverse process of energy-transfer upconversion

(ETU), $^3F_4(Tm_1) + {}^3F_4(Tm_2) \rightarrow {}^3H_6(Tm_1) + {}^3H_4(Tm_2)$. The CR depopulates the upper laser level while the ETU brings the ions back using the metastable $^3F_4$ state as a "reservoir" of electronic excitations. Thus, contrary to the ~1.9 μm laser transition, ETU plays a positive role for the ~2.3 μm lasers, while the CR is a detrimental effect. The pump quantum efficiency η_{q2}, defined as the number of electronic excitations to the $^3H_4$ level per number of absorbed pump photons at ~0.8 μm, can thus vary in the range of $0 < \eta_{q2} < 2$, where values below unity are governed by CR (assuming no ETU) and values above unity indicate efficient ETU.

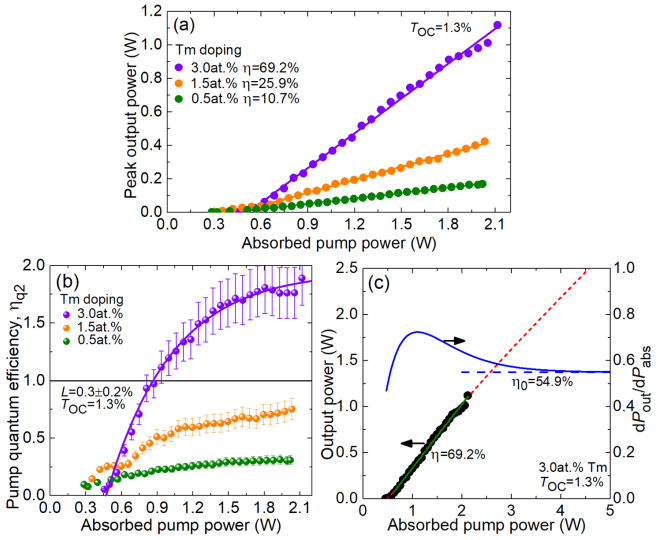

Fig. 13. Effect of doping concentration on the performance of Tm lasers operating on the $^3H_4 \rightarrow {}^3H_5$ transition: (a) input-output dependences, η – slope efficiency; (b) pump quantum efficiency η_{q2}: *symbols* – data calculated using Eq. (6), *violet curve* – empirical fit; (c) Output power and slope efficiency for 3 at.% Tm doped crystal: *circles* – experimental data on the output power, *green line* – their linear fit yielding experimental η, *red dashed curve* – extrapolated output power calculated using Eq. (6), *blue curve* – dP_{out}/dP_{abs}, Eq. (7), *dashed blue line* – the intrinsic slope efficiency η_0, Eq. (8). T_{OC} = 1.3%, λ_P = 793.8 nm, pump polarization: $\boldsymbol{E_P} \parallel N_p$. Quasi-CW operation (duty cycle: 1:2).

The pump quantum efficiency η_{q2} can be evaluated from the input-output dependence according to the following analytical equation [25]:

$$P_{out} = \frac{h\nu_L}{h\nu_P}\frac{w_L^2}{w_P^2}\frac{T_{OC}}{T_{OC}+L}\eta_{q2}P_{abs} - \frac{T_{OC}h\nu_L\pi w_L^2}{2\sigma_{SE}^L\tau_{30}}. \quad (6)$$

where P_{out} and P_{abs} are the output laser power and the absorbed pump power, respectively, h is the Planck constant, ν_L and ν_P are the laser and pump frequencies, respectively. The results on η_{q2} obtained using a round-trip loss L = 0.3±0.2% are shown in Fig. 13(c). The L value was taken to be slightly smaller than that estimated in Section 4C because of the longer laser wavelength and the lack of reabsorption. For all the studied Tm concentrations, the pump quantum efficiency gradually increases with the pump power and this dependence saturates well above the laser threshold. This can be explained as follows. In laser operation on the $^3H_4 \rightarrow {}^3H_5$ transition, the inversion rate is clamped by the condition "gain equals losses". However, the absolute population density of the $^3F_4$ state is not fixed and grows with the pump power. Indeed, direct measurements of the pump absorption under lasing conditions in ~2.3 μm Tm lasers indicate ground-state bleaching above threshold [25]. Thus, the rate of the ETU process which is proportional to the squared population density of the $^3F_4$ state increases with the pump power. This may be partially responsible for the nonlinear input-output dependences of the laser (another reason is the spatially non-uniform gain). At high pump powers well above the laser threshold, η_{q2} reaches a pump-independent value determined by a counteraction of CR and ETU leading to a linear output dependence.

Another observation is that for small Tm doping levels (0.5-1.5 at.%), η_{q2} is below unity. For the medium doping of 3 at.% Tm, it approaches 1.8±0.1, which explains the observed high laser efficiency. Moreover, with increasing Tm concentration, the maximum pump quantum efficiency gradually increases. It seems that the positive effect of ETU on the performance of ~2.3 μm lasers based on Tm:$KLu(WO_4)_2$ crystals is enhanced with the Tm doping concentration faster than the negative effect of CR.

Let us discuss the definition of the slope efficiency of a Tm laser operating on the $^3H_4 \rightarrow {}^3H_5$ transition. By definition, $\eta \equiv dP_{out}/dP_{abs}$. If the input-output dependence is linear within a certain range of pump powers, this will lead to a constant η value. By applying this definition to Eq. (6), we achieve:

$$\frac{dP_{out}}{dP_{abs}} = \eta_{St,L}\eta_{mode}\eta_{OC}\left(\eta_{q2}(P_{abs}) + \frac{d\eta_{q2}}{dP_{abs}}P_{abs}\right). \quad (7)$$

Here, η_{mode} is the mode overlap efficiency and η_{OC} is the output-coupling efficiency. As the pump quantum efficiency for the $^3H_4 \rightarrow {}^3H_5$ transition η_{q2} is pump-dependent, cf. Fig. 13(b), dP_{out}/dP_{abs} is not constant. For high pump powers well exceeding the laser threshold, the power dependence of η_{q2} is saturated ($\eta_{q2} \rightarrow \eta_{q2,0}$), so that:

$$\eta_0 = \left.\frac{dP_{out}}{dP_{abs}}\right|_{P_{abs} >> P_{th}} = \eta_{St,L}\eta_{mode}\eta_{OC}\eta_{q2,0}. \quad (8)$$

This equation gives a well-known definition of the laser slope efficiency.

In Fig. 13(c), we extrapolated the output power of the Tm laser using Eq. (6) and fitting the data on the pump quantum efficiency using an empirical formula $\eta_{q2} = \eta_{q2,0}$*exp[-(P_{abs} - P_{th})/P_0] where P_0 is a free parameter, as shown in Fig. 13(b). The result of this extrapolation is shown by the red dashed curve. Accordingly, we determine dP_{out}/dP_{abs} using Eq. (7), as shown by the blue solid curve. dP_{out}/dP_{abs} first increases above the laser threshold and then decreases asymptotically reaching the value of η_0 which is determined by Eq. (8). For the considered laser, η_0 = 54.9±3%. Note that this value is almost not sensitive to the round-trip passive loss used for the calculations. η_0 can be further improved under the condition of η_{mode} and η_{OC} both approaching unity (excellent mode-matching and very low round-trip intracavity losses), so that:

$$\eta_0 \le 2\eta_{St,L}. \quad (9)$$

This equation represents an upper limit for the slope efficiency of a Tm laser operating on the $^3H_4 \rightarrow {}^3H_5$ transition and represents an ideal two-for-one pump process.

F. The $^3H_4 \rightarrow {}^3H_5$ transition: Comparison with other hosts

So far, CW laser operation on the $^3H_4 \rightarrow {}^3H_5$ transition has been achieved in very few Tm^{3+}-doped fluoride ($LiYF_4$ [25], KY_3F_{10} [26,54]), BaY_2F_8 [55] and oxide ($Y_3Al_5O_{12}$ [29], $YAlO_3$ [30,56]) crystals. Among these results, we selected only those relying on laser-pumping at ~0.8 μm (to the $^3H_4$ state, conventional pump scheme). For this, typically, a Ti:Sapphire laser has been used as a pump source. The best results selected from publications on the topic are summarized in Table 3 highlighting the Tm doping level, the maximum phonon frequency of the host matrix $h\nu_{ph}$, the spectroscopic properties at the laser wavelength and the CW laser performance.

The Tm:$KLu(WO_4)_2$ crystal features the highest maximum phonon frequency (907 cm^{-1}) among the crystals intended for ~2.3 μm Tm

lasers. It also provides the highest SE cross-section for the $^3H_4 \rightarrow {}^3H_5$ transition in polarized light, owing to the strong polarization-anisotropy of spectroscopic properties of this monoclinic crystal, and relatively short radiative lifetime of the upper laser level. Moreover, we report on the highest output power and slope efficiency ever achieved from a laser-pumped ~2.3 μm Tm laser using a 3.0 at.% Tm:$KLu(WO_4)_2$ crystal. The slope efficiency (69.2%) almost approaches the limit set by two times the Stokes efficiency highlighting the very efficient ETU in this material.

An important parameter of the laser host crystal to be included in the comparison is the thermal conductivity κ. Its mean value for $KLu(WO_4)_2$ is $\langle\kappa\rangle$ = 3.12 $Wm^{-1}K^{-1}$ [58]. This value is lower than for other crystals considered in Table 3. Thus, thermal management of Tm lasers based on this crystalline host is very important.

Note that for pumping in the same absorption band of Tm^{3+} ($^3H_6 \rightarrow {}^3H_4$), AlGaAs laser diodes can be also used [59,60]. The main issues for diode-pumped ~2.3 μm Tm lasers (as compared to those pumped by high-brightness sources such as bulk or fiber lasers) are: (i) higher laser thresholds, (ii) the key role of optimized mode-matching between the pump and laser radiation preventing the appearance of higher-order modes and colasing at ~1.9 μm, (iii) more serious thermal effects in the active element.

Table 3. Summary[a] of Laser-pumped Thulium Lasers Operating on the $^3H_4 \rightarrow {}^3H_5$ Transition Reported So Far

Crystal[b]	Tm, at.%	$h\nu_{ph}$, cm^{-1}	σ_{SE}, 10^{-20} cm^2	τ_{30}, ms	λ_P, nm	P_{th}, W	P_{out}, W	η, %	λ_L, μm	M^2	Polariz.	Ref.
Tm:$LiYF_4$	3.5	446	0.57	**2.30**	780	**0.39**	0.73[qCW]	47.3	2.31	-	$\boldsymbol{E} \perp \boldsymbol{c}$ (π)	[25]
Tm:KY_3F_{10}	5.0	495	0.34	1.90	773	0.82	0.84[CW]	53.8	2.34	2.1-2.3	unpolarized	[26]
Tm:BaY_2F_8	3.0	421	0.49 [57]	1.10	779	~0.12	0.10[CW]	12	2.29	1.1	$\boldsymbol{E} \perp$ X	[55]
Tm:$YAlO_3$	1.8	552	0.78	0.70	776	0.41	0.96[CW]	61.8	2.27	-	$\boldsymbol{E} \perp \boldsymbol{b}$	[56]
Tm:$Y_3Al_5O_{12}$	3.2	857	0.35	0.79	781	0.86	1.07[CW]	46.3	2.19, 2.32	3.4	unpolarized	[29]
Tm:$KLu(WO_4)_2$	3.0	**907**	**1.78**	0.24	793	0.45	**1.12**[CW]	**69.2**	2.22, 2.29	2.2-2.6	$\boldsymbol{E} \perp N_m$	[c]

[a] $h\nu_{ph}$ – highest phonon energy of the host matrix, σ_{SE} – peak stimulated-emission cross-section at ~2.3 μm, τ_{30} – intrinsic lifetime of the $^3H_4$ state, λ_P – pump wavelength, P_{th} – laser threshold, P_{out} – output power, η – slope efficiency, λ_L – laser wavelength. [b] Best results selected from multiple publications on the same crystal. [c] This work.

5. CONCLUSIONS

To conclude, solid-state lasers based on Tm^{3+}-doped materials and operating on the $^3H_4 \rightarrow {}^3H_5$ transition are excellent candidates for highly efficient coherent light sources in the short-wave infrared spectral range and, in particular, at ~2.3 μm. Contrary to well-established models, they are rather tolerant to such key parameters of the gain media as their phonon spectra and Tm doping levels. This is due to the relatively complex physical nature of the $^3H_4 \rightarrow {}^3H_5$ laser scheme affected by both cross-relaxation and energy-transfer upconversion between neighboring Tm^{3+} ions. We prove that highly-efficient lasing at ~2.3 μm (with a slope efficiency exceeding the Stokes limit) can be achieved even in high-phonon energy Tm^{3+}-doped crystals at moderate doping levels leading to a notable self-quenching of the upper laser level by CR. An evidence of two-for-one pump process associated with the energy-transfer upconversion refilling the upper laser level and probably with the gain at the vibronic sideband of the $^3F_4 \rightarrow {}^3H_6$ transition has been provided. A compact Tm:$KLu(WO_4)_2$ laser generated a watt-level output at ~2.22 and 2.29 μm (multi-color emission) with a slope efficiency of 69.2% – record-high for this type of lasers. Thus, it can be expected that other Tm^{3+}-doped oxide crystals may be also of practical importance for ~2.3 μm lasers by providing better power scaling or other laser wavelengths.

We also extend the understanding of the physical nature of emission at wavelengths lying between the $^3H_4 \rightarrow {}^3H_5$ and $^3F_4 \rightarrow {}^3H_6$ electronic transitions. First, we determined the SE cross-sections for Tm^{3+} ions in $KLu(WO_4)_2$ which reached 1.78×10^{-20} cm^2 at 2289 nm for the former transition representing the highest value among all the Tm^{3+}-doped materials (crystals, ceramics and glasses) studied so far. We were able to assign multiple observed laser lines lying between 2.14 – 2.30 μm to electronic transitions occurring between the Stark sub-levels of the $^3H_4$ and $^3H_5$ multiplets. We also showed that vibronic transitions bridge the gap between the $^3H_4 \rightarrow {}^3H_5$ and $^3F_4 \rightarrow {}^3H_6$ electronic transitions leading to a non-vanishing SE cross-section and, potentially, optical gain within this spectral range. Based on these studies, we were able to explain previous findings on vibronic Tm lasers. Our results indicate that Tm^{3+}-doped monoclinic double tungstate crystals may provide a continuously tunable laser emission over an ultra-broad spectral range of about 1.7 – 2.5 μm.

We highlight the suitability of Tm^{3+}-doped monoclinic double tungstates for femtosecond mode-locked lasers at ~2.3 μm based on their broad emission spectra (bandwidth exceeding 30 nm, not affected by the inversion rate). Another relevant conclusion of our work is the possible contribution of $^3H_4 \rightarrow {}^3H_5$ and $^3F_4 \rightarrow {}^3H_6$ related vibronic emissions to the very broad emission spectra of ML thulium lasers extending beyond 2 μm, observed so far in several crystals [61,62]. This should be clarified further, e.g., by comparing the resonant Raman and vibronic gain in such materials.

Further power scaling of monoclinic double tungstate based ~2.3 μm Tm lasers can be realized in several ways, i.e., (i) by using other pump sources, such as laser diodes at ~0.8 μm (for the conventional pump scheme), Er Raman fiber lasers emitting at ~1.6 μm (in-band pumping [63]) or Yb fiber lasers at ~1 μm (upconversion pumping [64], which would require the measurements of the excited-state absorption spectra), or (ii) by using short highly-doped samples (5 – 15 at.% Tm) for better pump absorption, pump and laser mode overlap and high slope efficiency. The latter approach will require a rate-equation modeling of the Tm^{3+} system involving the ETU and energy-migrations rate constants which are still unknown for monoclinic double tungstates. The power scaling will raise the question of the fractional heat loading under laser operation on the $^3H_4 \rightarrow {}^3H_5$ transition. Finally, as Tm^{3+}-doped monoclinic double tungstates provide a positive thermal lens for certain crystal cuts, microchip ~2.3 μm lasers should be feasible.

Funding. French Agence Nationale de la Recherche (ANR) (LabEx EMC3 (ANR-10-LABX-09-01), SPLENDID2 (ANR-19-CE08-0028)); European Community funds FEDER and the Normandie region (European project "NOVAMAT"). Spanish Government, MINECO (MAT2016-75716-C2-1-R (AEI/FEDER,UE), PID2019-108543RB-I00); Generalitat de Catalunya (2017SGR755).

Disclosures. The authors declare no conflicts of interest.

References

1. F. J. McAleavey, J. O'Gorman, J. F. Donegan, B. D. MacCraith, J. Hegarty, and G. Mazé, "Narrow linewidth, tunable Tm^{3+}-doped fluoride fiber laser for optical-based hydrocarbon gas sensing," IEEE J. Sel. Top. Quantum Electron. **3**(4), 1103–1111 (1997).
2. A. Garnache, A. Liu, L. Cerutti, and A. Campargue, "Intracavity laser absorption spectroscopy with a vertical external cavity surface emitting laser at 2.3 µm: Application to water and carbon dioxide", Chem. Phys. Lett. **416**(1-3), 22-27 (2005).
3. M. E. Webber, J. Wang, S. T. Sanders, D. S. Baer, and R. K. Hanson, "In situ combustion measurements of CO, CO_2, H_2O and temperature using diode laser absorption sensors," Proc. Combust. Inst. **28**(1), 407–413 (2000).
4. S. T. Fard, W. Hofmann, P. T. Fard, G. Bohm, M. Ortsiefer, E. Kwok, M.-C. Amann, and L. Chrostowski, "Optical absorption glucose measurements using 2.3 µm vertical-cavity semiconductor lasers," IEEE Photon. Technol. Lett. **20**(11), 930-932 (2008).
5. V. Petrov, "Frequency down-conversion of solid-state laser sources to the mid-infrared spectral range using non-oxide nonlinear crystals," Progr. Quantum Electron. **42**, 1–106 (2015).
6. S. Mirov, V. Fedorov, I. Moskalev, D. Martyshkin, and C. Kim, "Progress in Cr^{2+} and Fe^{2+} doped mid-IR laser materials," Laser Photon Rev. **4**(1), 21-41 (2010).
7. I. T. Sorokina, E. Sorokin, S. Mirov, V. Fedorov, V. Badikov, V. Panyutin, A. Di Lieto, and M. Tonelli, "Continuous-wave tunable Cr^{2+}:ZnS laser," Appl. Phys. B **74**(6), 607-611 (2002).
8. I. T. Sorokina, "Cr^{2+}-doped II–VI materials for lasers and nonlinear optics," Opt. Mater. **26**(4), 395-412 (2004).
9. N. Tolstik, E. Sorokin, and I. T. Sorokina, "Graphene mode-locked Cr:ZnS laser with 41 fs pulse duration," Opt. Express **22**(5), 5564-5571 (2014).
10. T. J. Carrig, G. J. Wagner, A. Sennaroglu, J. Y. Jeong, and C. R. Pollock, "Mode-locked Cr^{2+}:ZnSe laser," Opt. Lett. **25**(3), 168-170 (2000).
11. E. Geerlings, M. Rattunde, J. Schmitz, G. Kaufel, H. Zappe, and J. Wagner, "Widely tunable GaSb-based external cavity diode laser emitting around 2.3 µm," IEEE Photon. Technol. Lett. **18**(18), 1913-1915 (2006).
12. G. Boehm, A. Bachmann, J. Rosskopf, M. Ortsiefer, J. Chen, A. Hangauer, R. Meyer, R. Strzoda, and M.-C. Amann, "Comparison of InP-and GaSb-based VCSELs emitting at 2.3 µm suitable for carbon monoxide detection," J. Cryst. Growth **323**(1), 442-445 (2011).
13. L. Shterengas, G. L. Belenky, A. Gourevitch, D. Donetsky, J. G. Kim, R. U. Martinelli, and D. Westerfeld, "High-power 2.3-µm GaSb-based linear laser array," IEEE Photon. Technol. Lett. **16**(10), 2218-2220 (2004).
14. J. Caird, L. DeShazer, and J. Nella, "Characteristics of room-temperature 2.3-µm laser emission from Tm^{3+} in YAG and $YAlO_3$," IEEE J. Quantum Electron. **11**(11), 874-881 (1975).
15. R. Allen and L. Esterowitz, "CW diode pumped 2.3 µm fiber laser," Appl. Phys. Lett. **55**(8), 721-722 (1989).
16. R. C. Stoneman and L. Esterowitz, "Efficient, broadly tunable, laser-pumped Tm:YAG and Tm:YSGG cw lasers," Opt. Lett. **15**(9), 486-488 (1990).
17. K. van Dalfsen, S. Aravazhi, C. Grivas, S. M. García-Blanco, and M. Pollnau, "Thulium channel waveguide laser with 1.6 W of output power and ~80% slope efficiency," Opt. Lett. **39**(15), 4380-4383 (2014).
18. R. Soulard, M. Salhi, G. Brasse, P. Loiko, J.-L. Doualan, L. Guillemot, A. Braud, A. Tyazhev, A. Hideur, and P. Camy, "Laser operation of highly-doped Tm:$LiYF_4$ epitaxies: towards thin-disk lasers," Opt. Express **27**(6), 9287-9301 (2019).
19. I. Yorulmaz and A. Sennaroglu, "Low-threshold diode-pumped 2.3-µm Tm^{3+}: YLF lasers," IEEE J. Sel. Top. Quantum Electron. **24**(5), 1601007-1-7 (2018).
20. J. F. Pinto, L. Esterowitz, and G. H. Rosenblatt, "Tm^{3+}:YLF laser continuously tunable between 2.20 and 2.46 µm," Opt. Lett. **19**(12), 883-885 (1994).
21. R. M. El-Agmy and N. M. Al-Hosiny, "2.31 µm laser under up-conversion pumping at 1.064 µm in Tm^{3+}: ZBLAN fibre lasers," Electron. Lett. **46**(13), 936-937 (2010).
22. Ò. Silvestre, M. C. Pujol, M. Rico, F. Güell, M. Aguiló, and F. Díaz, "Thulium doped monoclinic $KLu(WO_4)_2$ single crystals: growth and spectroscopy," Appl. Phys. B **87**(4), 707–716 (2007).
23. R. Soulard, A. Tyazhev, J.-L. Doualan, A. Braud, A. Hideur, M. Laroche, B. Xu, and P. Camy, "2.3 µm Tm^{3+}:YLF mode-locked laser," Opt. Lett. **42**(18), 3534-3536 (2017).
24. F. Canbaz, I. Yorulmaz, and A. Sennaroglu, "Kerr-lens mode-locked 2.3-µm Tm^{3+}:YLF laser as a source of femtosecond pulses in the mid-infrared," Opt. Lett. **42**(19), 3964-3967 (2017).
25. P. Loiko, R. Soulard, L. Guillemot, G. Brasse, J.-L. Doulan, A. Braud, A. Tyazhev, A. Hideur, B. Guichardaz, F. Druon, and P. Camy, "Efficient Tm:$LiYF_4$ lasers at ~2.3 µm: effect of energy-transfer upconversion," IEEE J. Quantum Electron. **55**(6), 1700212-1-12 (2019).
26. L. Guillemot, P. Loiko, R. Soulard, A. Braud, J.-L. Doualan, A. Hideur, and P. Camy, "Close look on cubic Tm:KY_3F_{10} crystal for highly efficient lasing on the $^3H_4 \rightarrow {}^3H_5$ transition," Opt. Express **28**(3), 3451-3463 (2020).
27. L. Guillemot, P. Loiko, R. Soulard, A. Braud, J.-L. Doualan, A. Hideur, R. Moncorgé, and P. Camy, "Thulium laser at ~2.3 µm based on upconversion pumping," Opt. Lett. **44**(16), 4071-4074 (2019).
28. Y. Morova, M. Tonelli, V. Petrov, and A. Sennaroglu, "Upconversion pumping of a 2.3 µm Tm^{3+}:KY_3F_{10} laser with a 1064 nm ytterbium fiber laser," Opt. Lett. **45**(4), 931-934 (2020).
29. L. Guillemot, P. Loiko, E. Kifle, J.-L. Doualan, A. Braud, F. Starecki, T. Georges, J. Rouvillain, A. Hideur, and P. Camy, "Watt-level mid-infrared continuous-wave Tm:YAG laser operating on the $^3H_4 \rightarrow {}^3H_5$ transition," Opt. Mater. **101**, 109745-1-8 (2020).
30. L. Guillemot, P. Loiko, A. Braud, J.-L. Doualan, A. Hideur, M. Koselja, R. Moncorgé, and P. Camy, "Continuous-wave Tm:$YAlO_3$ laser at ~2.3 µm," Opt. Lett. **44**(20), 5077-5080 (2019).
31. V. Petrov, M. C. Pujol, X. Mateos, Ò. Silvestre, S. Rivier, M. Aguiló, R. M. Solé, J. Liu, U. Griebner, and F. Díaz, "Growth and properties of $KLu(WO_4)_2$, and novel ytterbium and thulium lasers based on this monoclinic crystalline host," Laser Photonics Rev. **1**(2), 179–212 (2007).
32. J. M. Serres, X. Mateos, P. Loiko, K. Yumashev, N. Kuleshov, V. Petrov, U. Griebner, M. Aguiló, and F. Díaz, "Diode-pumped microchip Tm:$KLu(WO_4)_2$ laser with more than 3 W of output power," Opt. Lett. **39**(14), 4247– 4250 (2014).
33. P. Loiko, J. M. Serres, X. Mateos, K. Yumashev, A. Yasukevich, V. Petrov, U. Griebner, M. Aguiló, and F. Díaz, "Subnanosecond Tm:KLuW microchip laser Q-switched by a Cr:ZnS saturable absorber," Opt. Lett. **40**(22), 5220-5223 (2015).
34. A. Schmidt, S. Y. Choi, D. I. Yeom, F. Rotermund, X. Mateos, M. Segura, F. Diaz, V. Petrov, and U. Griebner, "Femtosecond pulses near 2 µm from a Tm:KLuW laser mode-locked by a single-walled carbon nanotube saturable absorber," Appl. Phys. Express **5**(9), 092704-1-3 (2012).
35. A. A. Kaminskii, K. Ueda, H. E. Eichler, J. Findeisen, S. N. Bagayev, F. A. Kuznetsov, A. A. Pavlyuk, G. Boulon, and F. Bourgeois, "Monoclinic tungstates $KDy(WO_4)_2$ and $KLu(WO_4)_2$ - new $\chi^{(3)}$-active crystals for laser Raman shifters," Jpn. J. Appl. Phys. **37**(8A), L923-L926 (1998).
36. H. Scheife, G. Huber, E. Heumann, S. Bär, and E. Osiac, "Advances in up-conversion lasers based on Er^{3+} and Pr^{3+}," Opt. Mater. **26**(4), 365-374 (2004).
37. P. Loiko, P. Segonds, P. L. Inácio, A. Peña, J. Debray, D. Rytz, V. Filippov, K. Yumashev, M. C. Pujol, X. Mateos, M. Aguiló, F. Díaz, M. Eichhorn, and B. Boulanger, "Refined orientation of the optical axes as a function of wavelength in three monoclinic double tungstate crystals $KRE(WO_4)_2$ (RE = Gd, Y or Lu)," Opt. Mater. Express **6**(9), 2984-2990 (2016).

38. B. Aull and H. Jenssen, “Vibronic interactions in Nd:YAG resulting in nonreciprocity of absorption and stimulated emission cross sections,” IEEE J. Quantum Electron. **18**(5), 925-930 (1982).
39. A. Ellens, S. Schenker, A. Meijerink, and G. Blasse, “Vibronic transitions of Tm^{3+} in various lattices,” J. Lumin. **69**(1), 1–15 (1996).
40. W. F. Krupke, “Optical absorption and fluorescence intensities in several rare-earth-doped Y_2O_3 and LaF_3 single crystals,” Phys. Rev. **145**(1), 325-337 (1966).
41. F. Auzel, “Multiphonon-assisted anti-Stokes and Stokes fluorescence of triply ionized rare-earth ions,” Phys. Rev. B **13**(7), 2809–2817 (1976).
42. A. Braud, S. Girard, J. L. Doualan, R. Moncorge, “Spectroscopy and fluorescence dynamics of (Tm^{3+},Tb^{3+}) and (Tm^{3+},Eu^{3+}) doped $LiYF_4$ single crystals for 1.5-µm laser operation,” IEEE J. Quantum Electron. **34**(11), 2246-2255 (1988).
43. X. Mateos, P. Loiko, J. M. Serres, K. Yumashev, U. Griebner, V. Petrov, M. Aguiló, and F. Díaz, “Efficient micro-lasers based on highly-doped monoclinic double tungstates,” IEEE J. Quantum Electron. **53**(3), 1700110-1-10 (2017).
44. P. Loiko, X. Mateos, S. Y. Choi, F. Rotermund, J. M. Serres, M. Aguiló, F. Díaz, K. Yumashev, U. Griebner, and V. Petrov, “Vibronic thulium laser at 2131 nm Q-switched by single-walled carbon nanotubes,” J. Opt. Soc. Am. B. **33**(11), D19-D27 (2016).
45. M. J. Weber, “Radiative and multiphonon relaxation of rare-earth ions in Y_2O_3,” Phys. Rev. **171**(2), 283-291 (1968).
46. C. B. Layne, W. H. Lowdermilk, and M. J. Weber, “Multiphonon relaxation of rare-earth ions in oxide glasses,” Phys. Rev. B **16**(1), 10-20 (1977).
47. J. M. de Mendívil, G. Lifante, M. C. Pujol, M. Aguiló, F. Díaz, and E. Cantelar, “Judd–Ofelt analysis and transition probabilities of Er^{3+} doped $KY_{1-x-y}Gd_xLu_y(WO_4)_2$ crystals,” J. Lumin. **165**, 153-158 (2015).
48. M. C. Pujol, M. Rico, C. Zaldo, R. Solé, V. Nikolov, X. Solans, M. Aguiló, and F. Díaz, “Crystalline structure and optical spectroscopy of Er^{3+}-doped $KGd(WO_4)_2$ single crystals,” Appl. Phys. B **68**(2), 187-197 (1999).
49. M. C. Pujol, J. Massons, M. Aguiló, F. Díaz, M. Rico, and C. Zaldo, “Emission cross sections and spectroscopy of Ho^{3+} laser channels in $KGd(WO_4)_2$ single crystal,” IEEE J. Quantum Electron. **38**(1), 93-100 (2002).
50. A. A. Demidovich, A. N. Kuzmin, N. K. Nikeenko, A. N. Titov, M. Mond, and S. Kueck, “Optical characterization of Yb,Tm:KYW crystal concerning laser application,” J. Alloys Compd. **341**(1-2), 124-129 (2002).
51. F. Güell, X. Mateos, Jna. Gavaldà, R. Sole, M. Aguiló, F. Dıaz, and J. Massons, “Blue luminescence in Tm^{3+}-doped $KGd(WO_4)_2$ single crystals,” J. Lumin. **106**(2), 109-114 (2004).
52. P. Loiko and M. Pollnau, “Stochastic model of energy-transfer processes among rare-earth ions. Example of Al_2O_3:Tm^{3+},” J. Phys. Chem. C **120**(46), 26480-26489 (2016).
53. J. A. Caird, S. A. Payne, P. R. Staber, A. J. Ramponi, L. L. Chase, and W. F. Krupke, “Quantum electronic properties of the $Na_3Ga_2Li_3F_{12}$:Cr^{3+} laser,” IEEE J. Quantum Electron. **24**(6), 1077–1099 (1988).
54. A. Muti, M. Tonelli, V. Petrov, and A. Sennaroglu, "Continuous-wave mid-infrared laser operation of Tm^{3+}:KY_3F_{10} at 2.3 µm," Opt. Lett. **44**(13), 3242-3245 (2019).
55. A. Muti, I. Baylam, M. Tonelli, and A. Sennaroglu, "Tunable continuous-wave laser operation of Tm^{3+}:BaY_2F_8 near 2.3 µm," Opt. Lett. **45**(15), 4104-4107 (2020).
56. L. Guillemot, P. Loiko, E. Kifle, A. Braud, J.-L. Doualan, A. Hideur, M. Koselja, R. Moncorgé, and P. Camy, “Spectroscopy and laser operation of Tm^{3+}:$YAlO_3$ crystal on the $^3H_4 \rightarrow {}^3H_5$ transition,” Proc. SPIE **11357**, 113570H-1-9 (2020).
57. P. Loiko, J. L. Doualan, L. Guillemot, R. Moncorgé, F. Starecki, A. Benayad, E. Dunina, A. Kornienko, L. Fomicheva, A. Braud, and P. Camy, “Emission properties of Tm^{3+}-doped CaF_2, KY_3F_{10}, $LiYF_4$, $LiLuF_4$ and BaY_2F_8 crystals at 1.5 µm and 2.3 µm,” J. Lumin. **225**, 117279-1-10 (2020).
58. Ò. Silvestre, J. Grau, M. C. Pujol, J. Massons, M. Aguiló, F. Díaz, M. T. Borowiec, A. Szewczyk, M. U. Gutowska, M. Massot, A. Salazar, and V. Petrov, "Thermal properties of monoclinic $KLu(WO_4)_2$ as a promising solid state laser host," Opt. Express **16**(7), 5022-5034 (2008).
59. S. Wang, H. Huang, H. Chen, X. Liu, S. Liu, J. Xu, and D. Shen, "High efficiency nanosecond passively Q-switched 2.3 µm Tm:YLF laser using a $ReSe_2$-based saturable output coupler," OSA Continuum **2**(5), 1676-1682 (2019).
60. E. Kifle, P. Loiko, L. Guillemot, J.-L. Doualan, F. Starecki, A. Braud, T. Georges, J. Rouvillain, and P. Camy, "Watt-level diode-pumped thulium lasers around 2.3 µm," Appl. Opt. **59**(25), 7530-7539 (2020).
61. Z. Pan, Y. Wang, Y. Zhao, H. Yuan, X. Dai, H. Cai, J. E. Bae, S. Y. Choi, F. Rotermund, X. Mateos, J. M. Serres, P. Loiko, U. Griebner, and V. Petrov, "Generation of 84-fs pulses from a mode-locked Tm:CNNGG disordered garnet crystal laser," Photon. Res. **6**(8), 800-804 (2018).
62. Y. Wang, W. Chen, M. Mero, L. Zhang, H. Lin, Z. Lin, G. Zhang, F. Rotermund, Y. J. Cho, P. Loiko, X. Mateos, U. Griebner, and V. Petrov, "Sub-100 fs Tm:$MgWO_4$ laser at 2017 nm mode locked by a graphene saturable absorber," Opt. Lett. **42**(16), 3076-3079 (2017).
63. P. Loiko, R. Thouroude, R. Soulard, L. Guillemot, G. Brasse, B. Guichardaz, A. Braud, A. Hideur, M. Laroche, H. Gilles, and P. Camy, "In-band pumping of Tm:$LiYF_4$ channel waveguide: a power scaling strategy for ~2 µm waveguide lasers," Opt. Lett. **44**(12), 3010-3013 (2019).
64. A. Tyazhev, F. Starecki, S. Cozic, P. Loiko, L. Guillemot, A. Braud, F. Joulain, M. Tang, T. Godin, A. Hideur, and P. Camy, "Watt-level efficient 2.3 µm thulium fluoride fiber laser," Opt. Lett. **45**(20), 5788-5791 (2020).